ORIGINAL ARTICLE

SnO₂ quantum dots modified N-doped carbon as high-performance anode for lithium ion batteries by enhanced pseudocapacitance

Cui-Ping Wu, Kai-Xuan Xie, Jia-Peng He, Qing-Peng Wang* ⓘ **,**
Jian-Min Ma* ⓘ **, Shun Yang, Qing-Hong Wang*** ⓘ

Abstract SnO₂ is considered to be a promising candidate as anode material for lithium ion batteries, due to its high theoretical specific capacity (1494 mAh·g⁻¹). Nevertheless, SnO₂-based anodes suffer from poor electronic conductivity and serious volume variation (300%) during lithiation/delithiation process, leading to fast capacity fading. To solve these problems, SnO₂ quantum dots modified N-doped carbon spheres (SnO₂ QDs@N–C) are fabricated by facile hydrolysis process of SnCl₂, accompanied with the polymerization of polypyrrole (PPy), followed by a calcination method. When used as anodes for lithium ion batteries, SnO₂ QDs@N–C exhibits high discharge capacity, superior rate properties as well as good cyclability. The carbon matrix completely encapsulates the SnO₂ quantum dots, preventing the aggregation and

volume change during cycling. Furthermore, the high N content produces abundant defects in carbon matrix. It is worth noting that SnO₂ QDs@N–C shows excellent capacitive contribution properties, which may be due to the ultra-small size of SnO₂ and high conductivity of the carbon matrix.

Keywords Tin dioxide; Quantum dots; Nitrogen-doped carbon; Lithium ion batteries

C.-P. Wu, K.-X. Xie, J.-P. He, S. Yang, Q.-H. Wang*
School of Chemistry and Materials Science, Jiangsu Normal University, Xuzhou 221116, China
e-mail: wangqh@jsnu.edu.cn

Q.-P. Wang*
Institute of Biopharmaceutical Research, Liaocheng University, Liaocheng 252059, China
e-mail: lywqp@126.com

J.-M. Ma*
School of Physics and Electronics, Hunan University, Changsha 410082, China
e-mail: nanoelechem@hnu.edu.cn

J.-M. Ma
Key Laboratory of Materials Processing and Mold (Zhengzhou University), Ministry of Education, Zhengzhou University, Zhengzhou 450002, China

1 Introduction

Excessive exhaustion of fossil resource has caused serious energy crisis and environmental damage. Therefore, exploiting/refining high-performance energy storage/conversion systems is of great importance [1]. Lithium ion batteries (LIBs) have become dominant among energy storage devices due to the advantages of high energy density and long cycle life [2–4]. However, the electrochemical performance of commercial LIBs is largely limited by the low specific capacity of graphite anode (theoretical capacity is 372 mAh·g⁻¹) and poor rate performance [5]. SnO₂ is presumed extraordinarily promising electrode material due to its high theoretical specific capacity (1494 mAh·g⁻¹) and environmental friendliness. Nevertheless, SnO₂-based anodes suffer from poor electronic conductivity and serious volume variation (300%) during lithiation/delithiation process, resulting in fast capacity fading [6–9]. To solve these problems, various strategies have been developed.

Tailoring specific nanostructures [10], such as nanoparticles, one-dimensional (1D) nanorods [11–13], two-dimensional (2D) nanosheets [14] and three-

dimensional (3D) nanoflowers [15] are commonly employed to improve the specific capacity and cycling performance of electrode materials. It is known that ultra-small particle size endows materials with high surface areas, which is beneficial for the fully contact between electrolyte and active nanoparticles. Thus, metal oxide quantum dots have been widely investigated as anode materials. For instance, Huang et al. [16] have prepared SnO$_2$ quantum dots/reduced graphene oxide composite and obtained high reversible capacity of 797 mAh·g^{-1} at 100 mA·g^{-1}, as well as long cycling life. However, ultra-fine particle size often causes aggregation of nanoparticles during the preparation process, as well as the redox process due to the high surface energy, thus leading to fast capacity attenuation. Therefore, the uniform dispersion and outstanding structure stability are key factors to make full use of quantum dots.

Combined with various carbon matrices, such as carbon nanotubes (CNTs) [17], graphene [18] and porous carbon [19] is commonly used to prevent the aggregation of nanoparticles. Moreover, carbon materials could act as soft media to reduce the stress of volume expansion and improve the electrical conductivity of electrode materials [20–25]. Therefore, various SnO$_2$/CNTs, SnO$_2$ quantum dots on reduced graphene oxide (SnO$_2$ QDs@RGO) and SnO$_2$ quantum dots on Ti$_3$C$_2$T$_x$ MXene (SnO$_2$ QDs/MXene) composites have been successfully fabricated and delivered superior lithium storage properties [26–28]. Cheng et al. [29] explored SnO$_2$@CNTs composites with controllable Sn–C bonding content via a hydrothermal method and subsequent annealing treatment. The SnO$_2$@CNTs with high Sn–C bonds content exhibit superior cycling stability and reversible capacity, which display the reversible capacity of ∼ 600 mAh·g^{-1} until 400 cycles at 200 mA·g^{-1}. It is noted that most reported SnO$_2$-based materials possess large particle size or suffer from serious aggregation. Fabrication of SnO$_2$ quantum dots modified carbon composites with perfect dispersion is still a big challenge.

Herein, SnO$_2$ quantum dots embedded in N-doped carbon spheres (SnO$_2$ QDs@N–C) are obtained by facile hydrolysis-high temperature calcination method using SnCl$_2$ and pyrrole monomer as starting materials. The hydrolysis of SnCl$_2$ and polyreaction of pyrrole monomer proceed at the same process, thus realized the uniform dispersion of Sn specie in the carbon precursor. The as-obtained SnO$_2$ QDs@N–C structure possesses multiple advantages. (1) The carbon matrix completely encapsulates the SnO$_2$ quantum dots, preventing their aggregation and volume change during cycling. (2) The superfine nanoparticles SnO$_2$ significantly decreases the diffusion distance for both ions and electrons, thence achieving improved rate capability [30]. (3) High N doping produces

much defects in carbon and increases the active sites for ion storage [31, 32]. Combining these advantages, the SnO$_2$ QDs@N–C composite shows an excellent rate capability (456.8 mAh·g^{-1} at 2 A·g^{-1}) and long cycle life (471.6 mAh·g^{-1} at 1A·g^{-1} after 400 cycles) for LIBs. The synthesis approach can be extended to the preparation of other metal oxide QDs/N–C composites.

2 Experimental

2.1 Materials preparation

The SnO$_2$ QDs@N–C composite was synthesized through a liquid-phase process and a subsequent high temperature calcination method. In a typical process, 0.15 g of tin(II) chloride hydrate was dissolved in 120 ml of deionized water under ice bath to form a clear solution. Then, pyrrole monomer (1 ml) was dropwise added into the above solution under magnetic stirring. Afterward, 0.6 g ammonium persulfate was added to the above solution. The hydrolysis of SnCl$_2$ and polymerization of pyrrole were implemented for 6 h under stirring. Then, Sn-polypyrrole (PPy) precursor was collected by filtration, washing and drying at 60 °C in a vacuum oven. Finally, the SnO$_2$ QDs@N–C composite was acquired by annealing the Sn-PPy precursor in Ar atmosphere for 2 h at 600 °C with the ramp rate of 2 °C·min^{-1}.

To investigate the effects of annealing temperature on the structures and morphologies of the products, parallel experiments were carried out. The temperatures were set to be 500, 600 and 700 °C, and the products were denoted to be SnO$_2$ QDs@N–C-500, SnO$_2$ QDs@N–C-600 and SnO$_2$ QDs@N–C-700, respectively.

2.2 Materials characterization

The structures of the SnO$_2$ QDs@N–C were characterized by powder X-ray diffraction (XRD, Bruker, D8 ADVANCE powder diffractometer, Cu Kα radiation, $\lambda = 0.15418$ nm). The surface morphologies were studied carefully using field-emission scanning electron microscope (FESEM, Hitachi SU8010). Transmission electron microscope (TEM, FEI, Tecnai G20) and high-resolution transmission electron microscope (HRTEM, FEI, Tecnai G20) equipped with an energy dispersive spectroscopy (EDS) were used to characterize the fine structures of samples. The oxidation states were confirmed by X-ray photoelectron spectroscopy (XPS, a VG Multilab 2000 (VG Inc.)) using monochromatic Al Kα radiation under vacuum of 2×10^{-6} Pa. The exact contents of Sn, C, N and O in composites were evaluated with inductive coupled plasma atomic emission spectroscopy (ICP-AES, USA

Themo Jarrel-Ash Corp.) and elemental analysis (EA, Perkin-Elmer 2400 Series II CHNS/O).

2.3 Electrochemical measurements

The working electrode was prepared by mixing the active materials, acetylene black and poly (vinyl difluoride), at a weight ratio of 70:20:10 in N-methyl-2-pyrrolidinone (NMP) solvent. The resulting slurry was pasted onto Cu foil and dried at 60 °C vacuum. The electrochemical tests were performed using CR 2032 coin half-cells. Lithium metal was served as the counter electrode, 1.0 mol·L^{-1} LiPF$_6$ dissolved in a mixture containing ethylene carbonate (EC), dimethyl carbonate (DMC), and propylene carbonate (PC) (4:5:1 by volume) was used as the electrolyte. The cells were assembled in an Ar-filled glove box. The cyclic voltammetry (CV) was performed on an electrochemical workstation (CHI 604E) in a potential range of 0.01−3.00 V at the scan rate of 0.1 mV·s^{-1} and electrochemical impedance spectroscopy (from 0.01 Hz to 100 kHz for the frequency range) measurements were conducted on a CHI604E electrochemical workstation. The galvanostatic charge–discharge curves, cycling stabilities and rate performances of the as-prepared SnO$_2$ QDs@N–C electrode were conducted on LAND CT 2001A battery testing system in a charge–discharge voltage window from 3.00 V to 0.01 V (vs. Li$^+$/Li).

3 Results and discussion

As illustrated in Scheme 1, SnO$_2$ QDs modified N-doped carbon spheres were prepared via a facile two-step method. The first process involves the hydrolysis of Sn specie and the chemical-polymerization of pyrrolemonomer. Sn (II) can be easily oxidized in to Sn (IV) precursor in the presence of ammonium persulfate and adsorbed on pyrrole ring due to the abundant N–H groups. Therefore, during the in-situ chemical-polymerization of pyrrolemonomer, the Sn (IV) species can be completely and uniformly

encapsuled in the PPy spheres to form Sn-PPy precursor (Fig. S1). During the subsequent annealing process, PPy was carbonized and Sn (IV) precursor was converted into SnO$_2$ QDs.

The crystal structures and oxidization states of the SnO$_2$ QDs@N–C composites were characterized by XRD and XPS measurements. As shown in Fig. 1a, all the as-prepared SnO$_2$ QDs@N–C samples display a broad peak at ∼ 25°, which can be indexed to the (002) plane of soft carbon. Upon increased temperature, the (002) peak shifts to a higher angle, indicating that the graphene interlayer space becomes smaller. Due to the ultra-small particle size and perfect encapsulation of N–C, no obvious peak of SnO$_2$ is observed.

The graphitization degree of the SnO$_2$ QDs@N–C composite was evaluated by Raman spectra. As shown in Fig. 1b, all the samples show two characteristic peaks located at 1367 and 1562 cm^{-1}, which are corresponding to the D-band and G-band of carbon materials, respectively. The spectra reveal that the intensity ratio of the G to D band (I_G/I_D) increases with calcination temperature, indicating an increased graphitization degree of the carbon matrix.

From the XPS survey spectra of SnO$_2$ QDs@N–C-600, Sn, C, N, and O elements were clearly detected (Fig. 1c-f). In the high-resolution Sn 3d spectra, two characteristic signals appear at 486.8 and 495.2 eV, corresponding to the Sn 3d$_{5/2}$ and Sn 3d$_{3/2}$ peaks of Sn(IV), indicating the formation of SnO$_2$ quantum dots. The C 1s spectra present four peaks located at 284.5, 285.4, 287.5 and 289.2 eV, which can be indexed to the C−C, N-sp^{2}C, N-sp^{3}C and C = C, respectively. Two characteristic peaks of pyridinic N (∼ 398.3 eV) and pyrrolic N (∼ 400.5 eV) were detected in the N 1s spectra, which are highly chemically active. The elemental analysis demonstrates that the content of N is as high as 13.74 wt% in SnO$_2$ QDs@N–C-600, which may produce abundant defects in carbon matrix, and is expected to enhance the reversible capacity and improve the fast kinetics. Combined with ICP measurements, the contents of SnO$_2$ are determined to be 28.03 wt%, 31.28
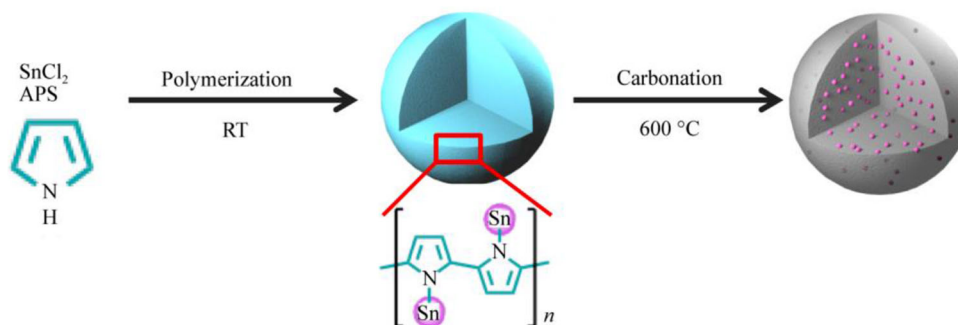
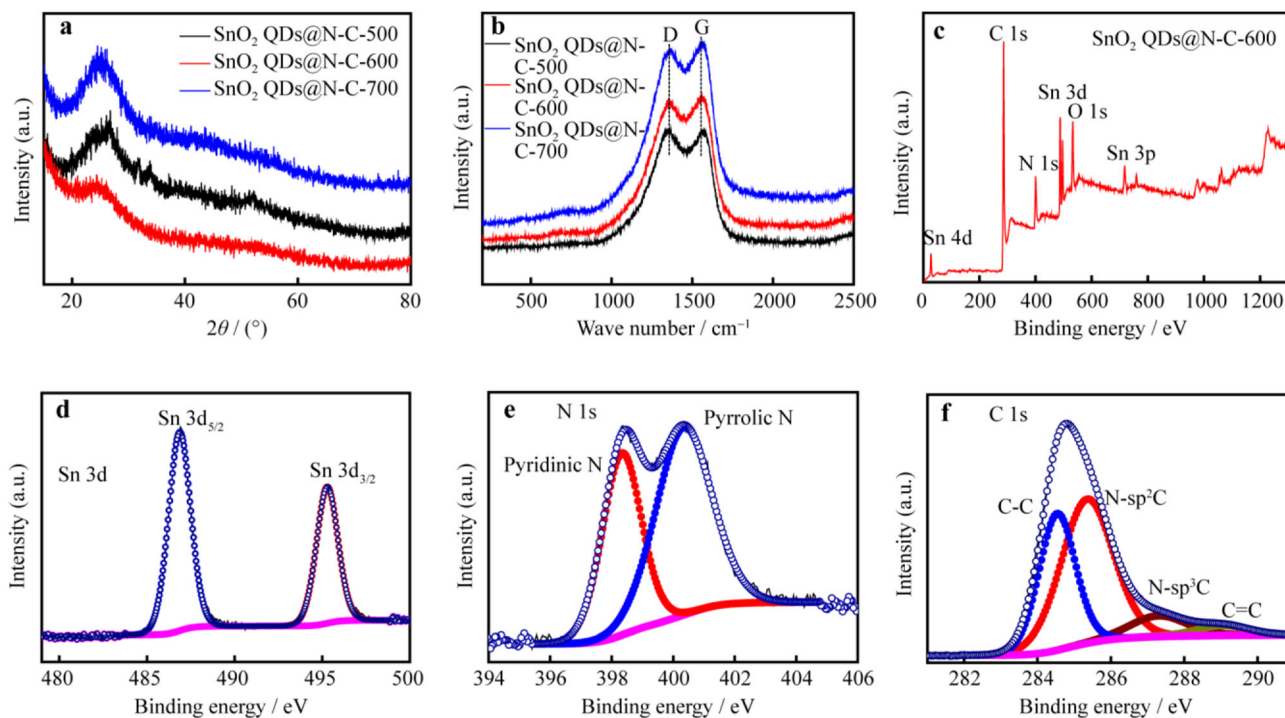**Scheme 1** Schematic illustration of SnO$_2$ QDs@N–C composite synthesis

Fig.1 a XRD patterns and **b** Raman spectra of SnO$_2$ QDs@N–C composites prepared at different temperatures; **c** XPS survey spectrum of SnO$_2$ QDs@N–C-600; high-resolution **d** Sn 3d, **e** N 1s and **f** C 1s spectra of SnO$_2$ QDs@N–C-600

wt% and 35.37 wt% in SnO$_2$ QDs@N–C-500, SnO$_2$ QDs@N–C-600 and SnO$_2$ QDs@N–C-700, respectively (Table S1). Moreover, it can be seen that N content is high in the carbon matrix, which may endow the carbon shell with high conductivity by creating abundant defects [33].

The morphologies of the as-prepared SnO$_2$ QDs@N–C samples were characterized by SEM, TEM and high-resolution TEM. As shown in Fig. 2a, b, the SnO$_2$ QDs@N–C-600 is composed of interconnected nanoparticles with ∼ 200 nm in diameter. The surfaces of the nanoparticles are rough, which may be beneficial for the fully infiltrates of electrolyte. High-resolution TEM images shown in Fig. 2c, d display that a mass of SnO$_2$ quantum dots uniformly disperse in the carbon matrix without aggregation or expose outside. Figure 2e shows that the diameter of the quantum dots is ∼ 2 nm. Selected area electron diffraction (SAED) pattern of SnO$_2$ QDs@N–C-600 (Fig. 2f) shows well-defined rings, indicating that the as-prepared sample is polycrystalline. The EDS elemental mapping of SnO$_2$ QDs@N–C-600 (Fig. 2g) demonstrates the incorporation of SnO$_2$ and its uniform distribution over the N–C spheres. SEM images shown in Fig. S1 demonstrate that other SnO$_2$ QDs@N–C samples obtained at different annealing temperatures all display similar sphere-like structures.

CV of the ultrafine SnO$_2$ QDs@N–C-600 electrode were measured at a sweep rate of 0.1 mV·s^{-1} in the voltage range of 0.01–3.00 V (vs. Li$^+$/Li). As show in Fig. 3a, in the initial cathodic sweep, the peak located at ∼ 0.352 V

could be assigned to the formation of a solid electrolyte interface (SEI) film, which is in accordance with the previous reports for SnO$_2$/carbon composite [34, 35]. In the following anodic process, a strong anodic peak appears at ∼ 0.615 V, demonstrating the dealloy reaction from Li$_x$Sn to Sn and Li. The other anodic peak observed at 1.143 V can be attributed to the conversion reaction from Sn to SnO$_2$. In the following cycles, the CV curves overlap well with each other, illustrating good cycling stability of the electrode.

Figure 3b shows the galvanostatic discharge/discharge performances of SnO$_2$ QDs@N–C-600 electrodes at 0.1 A·g^{-1} at the 1st, 2nd, 5th, 10th and 100th cycle. During the first discharge process, a quasi-plateau located between 0.5 and 1.0 V and a long tail extending to 0.01 V can be seen, which is consistent with the CV results. The initial discharge and charge capacities are 795.7 and 563.6 mAh·g^{-1} for SnO$_2$ QDs@N–C-500, 1435.9 and 1020.8 mAh·g^{-1} for SnO$_2$ QDs@N–C-600, and 940.5 and 638.9 mAh·g^{-1} for SnO$_2$ QDs@N–C-700, showing low first cycle coulombic efficiency of 70.8%, 71.1%, 67.9%, respectively. The irreversible capacity loss in the first cycle is caused by the formation of SEI films on the electrode surface and the decomposition of the electrolyte [36, 37]. From the second cycle, the charge/discharge profiles of different temperature SnO$_2$ QDs@N–C show a characteristic sloping feature, which is accord with previous report in N–C for LIBs [38]. After 6 cycles, the SnO$_2$ QDs@N–C-600 electrode
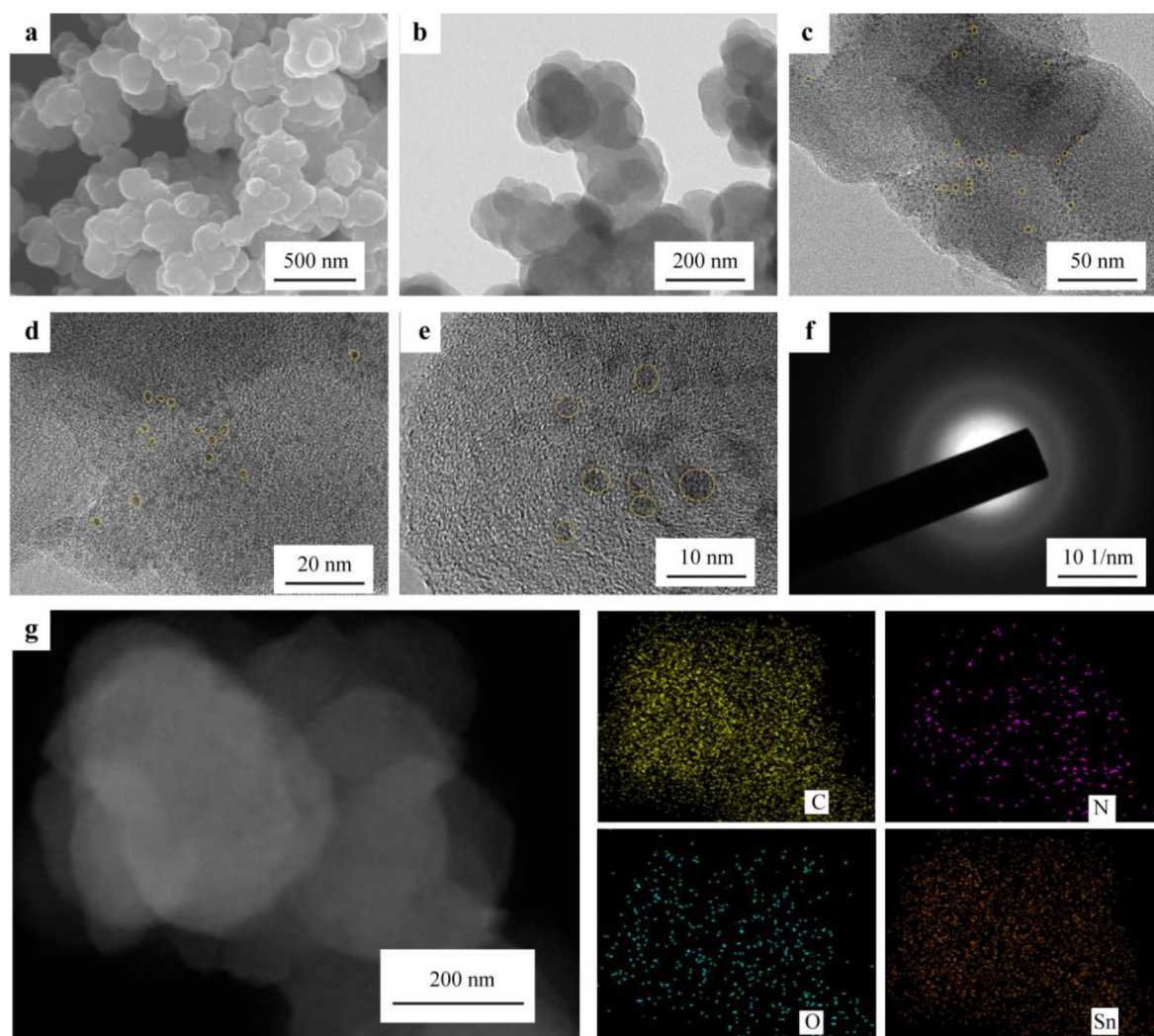
Fig.2 a SEM image, **b** TEM image, **c-e** HRTEM images, **f** SAED image, **g** TEM image and corresponding C, N, O and Sn elemental mappings of SnO$_2$ QDs@N–C-600 composite

exhibits more stable reversible capacity of 902.5 mAh·g^{-1} with high coulombic efficiency of ∼98%, which are higher than SnO$_2$ QDs@N–C-500 and SnO$_2$ QDs@N–C-700.

The SnO$_2$ QDs@N–C composites obtained at different temperatures all deliver excellent specific capacity at 0.1 A·g^{-1} (Fig. 3c). It is worth noting that the SnO$_2$ QDs@N–C-600 displays the highest specific capacity of 724.5 mAh·g^{-1} after 100 cycles. SnO$_2$ QDs@N–C-500, SnO$_2$ QDs@N–C-700 and N–C-600 deliver lower reversible capacities of 327.0, 552.5 and 500.0 mAh·g^{-1} after 100 cycles, respectively.

Rate capability is a significant indicator in assessing the high-power practical applications. Figure 3d elucidates the rate performances of the SnO$_2$ QDs@N–C electrodes under various current densities. When the current densities increase from 100, to 200, 500, 1000 and 2000 mA·g^{-1}, the specific capacities of SnO$_2$ QDs@N–C-600 are quantified as 855.8, 796.3 668.9, 574.0 and 456.8 mAh·g^{-1},

respectively. What's more, when the current density goes back to 0.1 A·g^{-1}, the specific capacity can be recovered to 763.8 mAh·g^{-1}, illustrating the good rate capability and excellent cycling stability of SnO$_2$ QDs@N–C-600.

To further investigate the cycling performances of the SnO$_2$ QDs@N–C composites, the as-prepared electrodes were measured at a higher current density (Fig. 3e). It can be found that SnO$_2$ QDs@N–C-600 delivers remarkably better cycling performance than SnO$_2$ QDs@N–C-500 and SnO$_2$ QDs@N–C-700 at a current density of 1 A·g^{-1}. After 400 cycles, the specific capacity of SnO$_2$ QDs@N–C-600 keeps 471.6 mAh·g^{-1}, showing superior cycling stability.

Furthermore, the outstanding electrochemical performance of the SnO$_2$ QDs@N–C-600 attracted attention to explore the electrochemical kinetics process. CV measurements of SnO$_2$ QDs@N–C-600 electrode were carried out at different sweep rates from 0.2 to 1.0 mV·s^{-1}. As
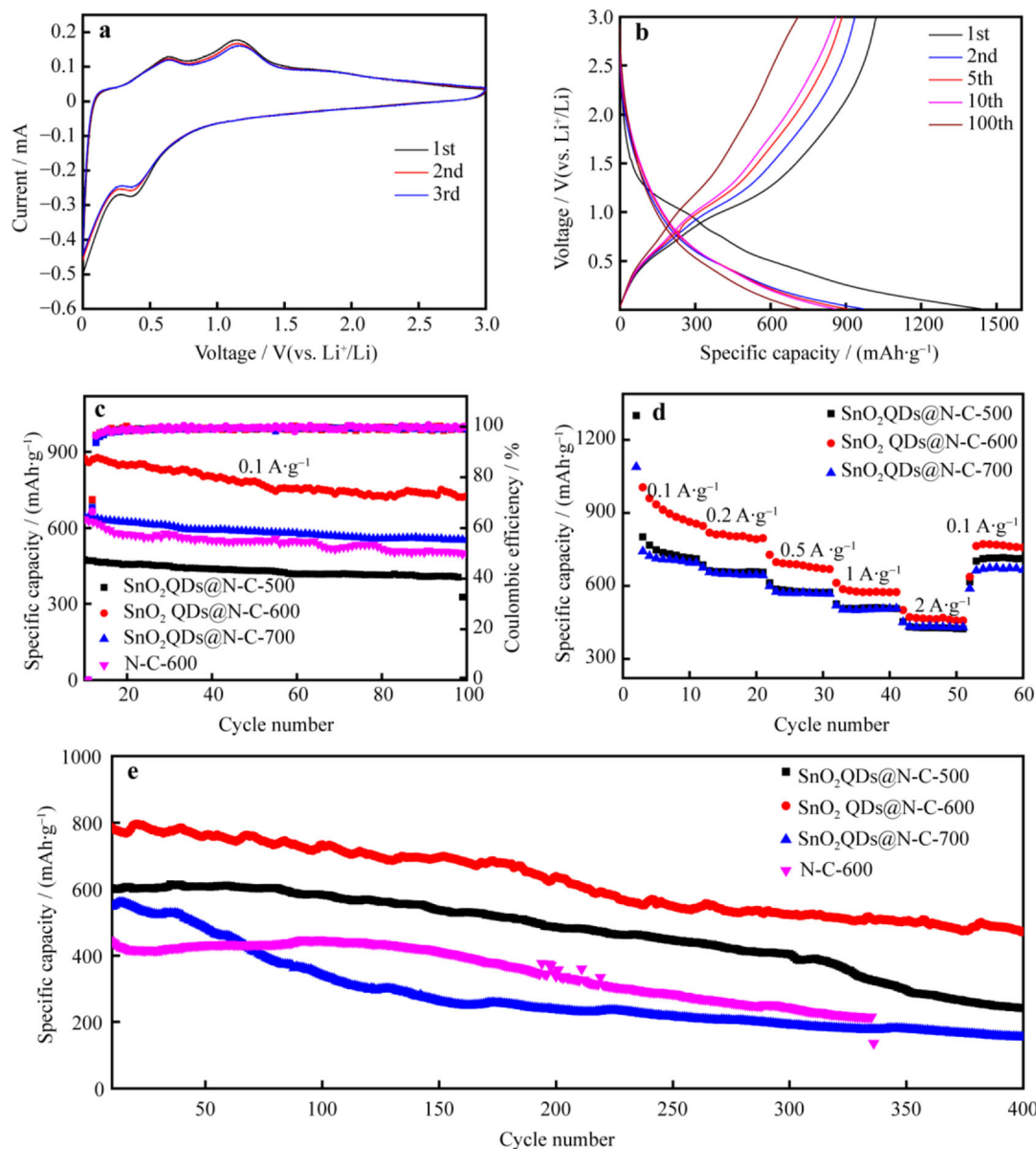
Fig. 3 **a** CV curves at a scanned rate of 0.1 mV·s⁻¹ and **b** discharge–charge voltage profiles measured at a current density of 0.1 A·g⁻¹ of SnO₂ QDs@N–C–600 electrodes; **c** cycling performances of SnO₂ QDs@N–C and N-C-600 electrodes at 0.1 A·g⁻¹; **d** rate performances of SnO₂ QDs@N–C electrodes at different current densities; **e** long-term cycling performances and coulombic efficiencies of SnO₂ QDs@N–C and N-C-600 electrodes at 1 A·g⁻¹

shown in Fig. 4a, the CV curves demonstrate similar shape at different scan rates, implying a small polarization voltage and fast kinetics. The obtained peaks current (i) and scan rate (v) obey the following equations [39]:

$$i = av^b \tag{1}$$

$$\lg i = \lg a + b \lg v \tag{2}$$

where a and b are constants. According to the previous studies, when the b value equals to 0.5 or 1 [30, 40, 41], the electrochemical reaction is dominantly diffusion controlled

or capacitive controlled, respectively. As shown in Fig. 4b, the calculated b values of the Peaks A, B and C are 0.782, 0.723 and 0.763, respectively, suggesting that both the pseudocapacitive behavior and ionic diffusion emerged during the Li storage process. Moreover, the overall capacitive contribution at a fixed scan rate was quantitatively analyzed by distinguishing the fraction of capacitive contribution (k_1v) and diffusion-limited contribution ($k_2v^{1/2}$) at a certain potential (V) according to the following relationships:
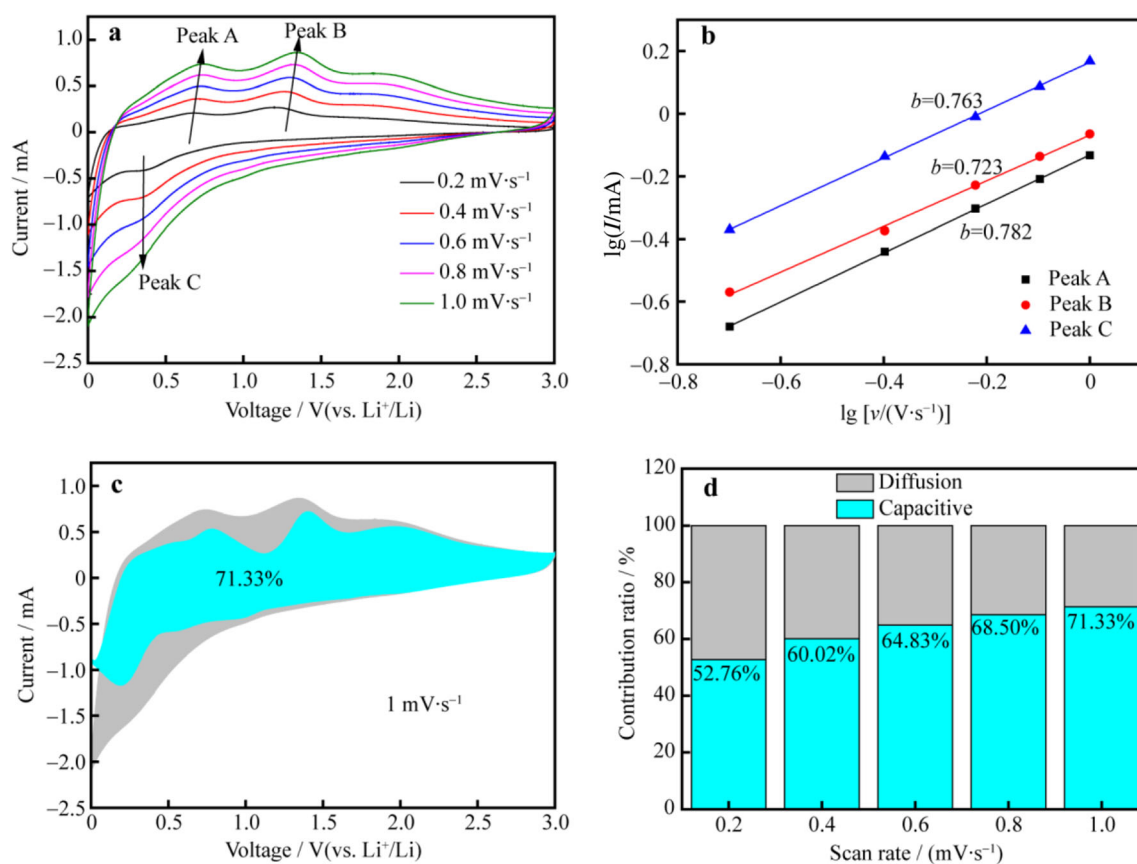
Fig.4 a CV curves of SnO_2 QDs@N–C-600 electrode for Li-ion storage at different scan rates from 0.2 to 1.0 mV·s^{-1}; **b** calculation of b values; **c** capacitive contribution curve of SnO_2 QDs@N–C-600 at a scan rate of 1.0 mV·s^{-1}; **d** contribution ratios of capacitive and diffusion-controlled capacities at increasing sweep rates from 0.2 to 1.0 mV·s^{-1}

$$i(V) = k_1 v + k_2 v^{1/2} \tag{3}$$

$$i(V)/v^{1/2} = k_1 v^{1/2} + k_2 \tag{4}$$

With the increase of sweep rate, the capacitive contribution of total charge storage gradually rises. The ratio of the capacitive contribution at a scan rate of 1.0 mV·s^{-1} is $\sim 71.33\%$ (Fig. 4c, d), indicating that capacitive process is dominant. The calculation results are also consistent with the results of b values. Scilicet the unique structure of the ultrafine SnO_2 QDs@N–C composite facilitates the pseudocapacitive process, thus resulting in a high reversible capacity and elevated rate performance.

Finally, the SnO_2@N–C-600 demonstrates the best electrochemical properties. The excellent performance may be ascribed to multiple advantages. Firstly, SnO_2 quantum dots not only decrease the diffusion length for ion/electrons, but also extremely improve the utilization of active substances due to uniform dispersion. Secondly, the carbon matrix completely encapsulates the SnO_2 quantum dots, relieves aggregation and volume change of SnO_2 during the lithiation-delithiation process. As shown in Fig. S2, the function of the carbon matrix is obvious. After 400 cycles,

the SnO_2 quantum dots are still embedded carbon spheres. Moreover, the electrode still maintains the intact structure and exhibits excellent specific capacity.

Thirdly, SnO_2 QDs@N–C are equipped with excellent conductivity. As shown in Fig. S3, the Nyquist plot consists of two semicircles and an approximately 45° slope. The high-frequency semicircle is related to the formation of SEI film. According to the fitted results (Table S$_2$), SnO_2 QDs@N–C-600 delivers the smallest SEI layer resistance (R_s), indicating its lowest contact resistance, which is of great benefit to electrode performance. The medium-frequency semicircle can be assigned to charge transfer resistance (R_{ct}) at the interface of the electrolyte/electrode. The R_{ct} values of SnO_2 QDs@N–C-500, SnO_2 QDs@N–C-600 and SnO_2 QDs@N–C-700 are 13.33, 11.12 and 8.59 Ω, respectively. Clearly, SnO_2 QDs@N–C all demonstrate small R_{ct}, which indicates superior capacitive performance and enhanced electronic conductivity by carbon materials. In the low frequency region, the sloping line is attribute to the Warburg impedance (W), which is related to Li-ion diffusion in the bulk electrode. The steep slope reveals an ideal capacitive behavior, which is in good agreement with the above results.

4 Conclusion

In summary, SnO$_2$ quantum dots modified N-doped carbon spheres are obtained by facile hydrolysis-high temperature calcination method using SnCl$_2$ and pyrrole monomer as precursors. As anodes for lithium ion batteries, the SnO$_2$ QDs@N–C-600 shows a high discharge capacity of 724.5 mAh·g^{-1} at 0.1 A·g^{-1} after 100 cycles and superior rate capability (456.8 mAh·g^{-1} at 2 A·g^{-1}), as well as excellent cycling stability (471.6 mAh·g^{-1} at 1 A·g^{-1} after 400 cycles). Excellent electrochemical performance is attributed to the satisfactory structure. The superfine nanoparticles SnO$_2$ significantly decreases the diffusion distance for ion/electrons, thence rate capability is improved. Then, N–C can create defects in carbons and increases the active sites for ion storage. Furthermore, the encapsulation structure of the carbon sphere is beneficial to enhance the structural stability. The decreased particles size and good conductivity are beneficial for the improvement of capacitive contribution. This work provides an effective way to obtain electrode materials with high specific capacity and good cycling performance for energy storage.

References

[1] Zou G, Hou H, Ge P, Huang Z, Zhao G, Yin D, Ji X. Metal-organic framework derived materials for sodium energy storage. Small. 2018;14(3):1702648.

[2] Sun L, Ma T, Zhang J, Guo X, Yan C, Liu X. Double-shelled hollow carbon spheres confining tin as high performance electrodes for lithium ion batteries. Electrochim Acta. 2019;321: 134672.

[3] Han Y, Huang G, Xu S. Structural reorganization–based nanomaterials as anodes for lithium-ion batteries: design, preparation, and performance. Small. 2019;16(15):1902841.

[4] Kim AY, Ardhi REA, Liu G, Kim GY, Shin HJ, Byun D, Lee JK. Hierarchical hollow dual core-shell carbon nanowall-encapsulated p-n SnO/SnO$_2$ heterostructured anode for high-performance lithium-ion-based energy storage. Carbon. 2019;153: 62.

[5] Zhang Y, Xia X, Liu B, Deng S, Xie D, Liu Q, Wang Y, Wu J, Wang X, Tu J. Multiscale graphene-based materials for applications in sodium ion batteries. Adv Energy Mater. 2019;9(8): 1803342.

[6] Han X, Li R, Qiu S, Zhang X, Zhang Q, Yang Y. Sonochemistry-enabled uniform coupling of SnO$_2$ nanocrystals with graphene sheets as anode materials for lithium-ion batteries. RSC Adv. 2019;9(11):5942.

[7] Du X, Yang T, Lin J, Feng T, Zhu J, Lu L, Xu Y, Wang J. Microwave-assisted synthesis of SnO$_2$@polypyrrole nanotubes and their pyrolyzed composite as anode for lithium-ion batteries. ACS Appl Mater Interfaces. 2016;8(24):15598.

[8] Huang S, Wang W, Chen D, Hu Z, Jiang Y, Chen Z, Li Z, Pan D, Zhao B. Enhancing lithium-ion batteries performance via electron-beam irradiation strategies: a case study of graphene aerogels loaded with SnO$_2$ quantum dots. Electrochim Acta. 2018;281(10):769.

[9] Li B, Yan Y, Shen C, Yu Y, Wang Q, Liu M. Extraordinary lithium ion storage capability achieved by SnO$_2$ nanocrystals with exposed {221} facets. Nanoscale. 2018;10(34):16217.

[10] Wu SJ, Wu ZH, Fang S, Qi SP, Yu B, Yang JY. A comparison of core-shell Si/C and embedded structure Si/C composites as negative materials for lithium-ion batteries. Rare Metal. 2019. https://doi.org/10.1007/s12598-019-01354-8.

[11] Zhang W, Sheng JZ, Zhang J, He T, Hu L, Wang R, Mai LQ, Mu SC. Hierarchical three-dimensional MnO nanorods/carbon anodes for ultralong-life lithium-ion batteries. J Mater Chem A. 2016;4(43):16936.

[12] Yang JL, Hu L, Zheng JX, He DP, Tian LL, Mu SC, Pan F. Li$_2$FeSiO$_4$ nanorods bonded with graphene for high performance batteries. J Mater Chem A. 2015;3(18):9601.

[13] Zhang Q, Liao J, Liao M, Dai J, Ge H, Duan T, Yao W. One-dimensional Fe$_7$S$_8$@C nanorods as anode materials for high-rate and longlife lithium-ion batteries. Appl Surf Sci. 2019; 473:799.

[14] Yao Y, Xiao Z, Liu P, Zhang S, Niu Y, Wu H, Liu S, Tu W, Luo Q, Sial MAZG. Facile synthesis of 2D ultrathin and ultrahigh specific surface hierarchical porous carbon nanosheets for advanced energy storage. Carbon. 2019;155:674.

[15] Li L, Ye M, Ding Y, Xie D, Yu D, Hu Y, Chen HY, Peng S. Controlled synthesis of porous CaCo$_2$O$_4$ nanoflowers and their multifunctional applications for lithium ion batteries and oxygen evolution reaction. J Alloy Compd. 2020;812:152099.

[16] Huang M, Feng M, Li H, Huang P, Su Q, Zhang F, Du G. Rapid microwave-assisted synthesis of SnO$_2$ quantum dots/reduced graphene oxide composite with its application in lithium-ion battery. Mater Lett. 2017;209:260.

[17] Wang J, Wang J, Han L, Liao C, Cai W, Kan Y, Hu Y. Fabrication of an anode composed of a N, S codoped carbon nanotube hollow architecture with CoS$_2$ confined within: toward Li and Na storage. Nanoscale. 2019;11(43):20996.

[18] Kumar R, Sahoo S, Joanni E, Singh RK, Tan WK, Kar KK, Matsuda A. Recent progress in the synthesis of graphene and derived materials for next generation electrodes of high performance lithium ion batteries. Prog Energ Combust. 2019;75: 100786.

[19] Yan Z, Yang Q, Wang Q, Ma J. Nitrogen doped porous carbon as excellent dual anodes for Li- and Na-ion batteries. Chinese Chem Lett. 2020;31(2):583.

[20] Wang Q, Zhang W, Guo C, Liu Y, Wang C, Guo Z. In situ construction of 3D interconnected FeS@Fe$_3$C@graphitic carbon networks for high-performance sodium-ion batteries. Adv Funct Mater. 2017;27(41):1703390.

[21] Liu Y, Yan Y, Li K, Yu Y, Wang Q, Liu M. A high-areal-capacity lithium-sulfur cathode achieved by a boron-doped carbon–sulfur aerogel with consecutive core-shell structures. Chem Commun. 2019;55(8):1084.

[22] Liu M, Yang Z, Sun H, Lai C, Zhao X, Peng H, Liu T. A hybrid carbon aerogel with both aligned and interconnected pores as interlayer for high-performance lithium–sulfur batteries. Nano Res. 2016;9(12):3735.

[23] Liu M, Zhang P, Qu Z, Yan Y, Lai C, Liu T, Zhang S. Conductive carbon nanofiber interpenetrated graphene architecture for ultra-stable sodium ion battery. Nat Commun. 2019;10(1):1.

[24] Yang Z, Zhang P, Wang J, Yan Y, Yu Y, Wang Q, Liu M. Hierarchical carbon@SnS$_2$ aerogel with "skeleton/skin"

architectures as a high-capacity, high-rate capability and long cycle life anode for sodium ion storage. ACS Appl Mater Interfaces. 2018;10(43):37434.

[25] Dong Y, Feng Y, Deng J, He P, Ma J. Electrospun Sb_2Se_3@C nanofibers with excellent lithium storage properties. Chinese Chem Lett. 2020; 31(3):909.

[26] Hu R, Sun W, Liu H, Zeng M, Zhu M. The fast filling of nano-SnO_2 in CNTs by vacuum absorption: a new approach to realize cyclic durable anodes for lithium ion batteries. Nanoscale. 2013;5(23):11971.

[27] Liu H, Zhang X, Zhu Y, Cao B, Zhu Q, Zhang P, Xu B, Wu F, Chen R. Electrostatic self-assembly of 0D–2D SnO_2 quantum dots/$Ti_3C_2T_x$ MXene hybrids as anode for lithium-ion batteries. Nano-Micro Lett. 2019;11(1):65.

[28] Ren L, Yao Y, Wang K, Li S, Zhu K, Liu J. Novel one-step in situ growth of SnO_2 quantum dots on reduced graphene oxide and its application for lithium ion batteries. J Solid State Chem. 2019;273:128.

[29] Cheng Y, Huang J, Qi H, Cao L, Luo X, Li J, Xu Z, Yang J. Controlling the Sn-C bonds content in SnO_2@CNTs composite to form in-situ pulverized structure for enhanced electrochemical kinetics. Nanoscale. 2017;9(47):18681.

[30] Yang H, Xu R, Yao Y, Ye S, Zhou X, Yu Y. Multicore-shell Bi@N-doped carbon nanospheres for high power density and long cycle life sodium- and potassium-ion anodes. Adv Funct Mater. 2019;29(13):1809195.

[31] Xu C, Niu D, Zheng N, Yu H, He J, Li Y. Facile synthesis of nitrogen-doped double-shelled hollow mesoporous carbon nanospheres as high-performance anode materials for lithium ion batteries. ACS Sustain Chem Eng. 2018;6(5):5999.

[32] Dai R, Sun W, Wang Y. Ultrasmall tin nanodots embedded in nitrogen-doped mesoporous carbon: metal-organic-framework derivation and electrochemical application as highly stable anode for lithium ion batteries. Electrochim Acta. 2016;217:123.

[33] Xu Y, Zhang C, Zhou M, Fu Q, Zhao C, Wu M, Lei Y. Highly nitrogen doped carbon nanofibers with superior rate capability and cyclability for potassium ion batteries. Nat Commun. 2018; 9(1):1720.

[34] Zhu C, Wei D, Wu Y, Zhang Z, Zhang G, Duan J, Li L, Zhu H, Zhu Z, Chen Z. Controllable construction of interconnected SnO_x/N-doped carbon/carbon composite for enhanced-performance lithium-ion batteries anodes. J Alloy Compd. 2019;778:731.

[35] Yuan J, Hao Y, Zhang X, Li X. Sandwiched CNT@SnO_2@PPy nanocomposites enhancing sodium storage. Colloids Surf A. 2018;555:795.

[36] Wang Y, Jin YH, Zhao CC, Duan YH, He XZ, Jia MQ. SnO_2 quantum dots/graphene aerogel composite as high-performance. Anode material for sodium ion batteries. Mat Lett. 2017;191:169.

[37] Xia SB, Yao LF, Guo H, ShenX LJM, Cheng FX, Liu JJ. Li^+ intercalcation pseudocapacitance in Sn-based metal-organic frameworkfor high capacity and ultra-stable Li ion storage. J Power Sources. 2019;440:227162.

[38] Liu X, Chao D, Li Y, Hao J, Liu X, Zhao J, Lin J, Fan HJ, Shen ZX. A low-cost and one-step synthesis of N-doped monolithic quasi-graphene films with porous carbon frameworks for Li-ion batteries. Nano Energy. 2015;17:43.

[39] Lu J, Xia G, Gong S, Wang C, Jiang P, Lin Z, Wang D, Yang Y, Chen Q. Metallic 1T phase MoS_2 nanosheets decorated hollow cobalt sulfide polyhedrons for high-performance lithium storage. J Mater Chem A. 2018;6(26):12613.

[40] He J, Shen L, Wu C, Guo C, Wang Q, Liu Z, Yang S, Wang Q. Rational design of Ni/Ni_2P heterostructures encapsulated in 3D porous carbon networks for improved lithium storage. Dalton T. 2019;48(42):16000.

[41] Wang Q, Zhu Y, Xue J, Zhao X, Guo Z, Wang C. General synthesis of porous mixed metal oxide hollow spheres with enhanced supercapacitive properties. ACS Appl Mater Interfaces. 2016;8(27):17226.